

Supporting information

Stable High Efficiency Two-Dimensional Perovskite Solar Cells *via* Cesium Doping

Xu Zhang,^{abc} Xiaodong Ren,^b Bin Liu,^b Rahim Munir,^d Xuejie Zhu,^b Dong Yang,^b Jianbo Li,^b Yucheng Liu,^b
5 Detlef-M. Smilgies,^e Ruipeng Li,^e Zhou Yang,^b Tianqi Niu,^b Xiuli Wang,^a Aram Amassian,^d Kui Zhao^{*b} and
Shengzhong (Frank) Liu^{*ab}

^aDalian National Laboratory for Clean Energy; iChEM, Dalian Institute of Chemical Physics, Chinese
Academy of Sciences, Dalian, 116023, China. E-mail: szliu@dicp.ac.cn

10 ^bKey Laboratory of Applied Surface and Colloid Chemistry, National Ministry of Education; Shaanxi Key
Laboratory for Advanced Energy Devices; Shaanxi Engineering Lab for Advanced Energy Technology,
School of Materials Science and Engineering, Shaanxi Normal University, Xi'an 710119, China. E-mail:
Zhaok@snnu.edu.cn

^cUniversity of Chinese Academy of Sciences, Beijing, 100049, China.

15 ^dKing Abdullah University of Science and Technology (KAUST), KAUST Solar Center (KSC) and Physical
Science and Engineering Division (PSE), Thuwal 23955-6900, Saudi Arabia

^eCornell High Energy Synchrotron Source (CHESS), Cornell University, Ithaca, NY 14853, U.S.A.

*Corresponding author: szliu@dicp.ac.cn; Zhaok@snnu.edu.cn

20

Experimental Section

Solution preparation and device fabrication

The perovskite solution was comprised of BAI (99.5%, Xi'an Polymer Light Technology Corp), MAI (99.5%, Xi'an Polymer Light Technology Corp), CsI (99.999%, Alfa Aesar) and PbI_2 (99.9985%, Alfa Aesar) (2 : 3-3x : 3x : 4 molar ratio) in mixed solvents of dimethylsulfoxide (DMSO, 99.9%, Aladdin) and N,N-dimethylformamide (DMF, 99.9%, Aladdin, 7:3 in volume) with concentration of 1.2 M. The spiro-OMeTAD solution was prepared by dissolving 90 mg spiro-OMeTAD, 22 μL lithium bis(trifluoromethanesulfonyl) imide (99%, Acros Organics, 520 mg mL^{-1}) in acetonitrile (99.7+%, Alfa Aesar) and 36 μL 4-tert-butylpyridine (96%, Aldrich) in 1 mL chlorobenzene (99.8%, Aldrich). All solutions were prepared under inert atmosphere inside a nitrogen glove box. The FTO-coated glass (2.5 cm * 2.5 cm) was cleaned by sequential sonication in acetone, isopropanol and ethanol for 30 min each and then dried under N_2 flow. The cleaned substrate was exposed to ultraviolet and ozone for 15 min before hot-casting. The spin-coating was accomplished under inert atmosphere inside a nitrogen glove box. The TiO_2 was prepared by chemical bath deposition with the FTO glass immersed in a TiCl_4 (CP, Sinopharm Chemical Reagent Co., Ltd) aqueous solution with the volume ratio of TiCl_4 : H_2O equal to 0.0225 : 1 at 70 °C for 1 hour. The FTO/ TiO_2 substrates were preheated at 100 °C for 10 min, followed by dropping 70 μL precursor solutions and spin-coating at 5000 r.p.m. for 20s without delay. The as-cast films were then annealed at 100 °C for 10 minutes.

The hole-transporting layer was deposited onto the light-absorbing layer by spin-coating spiro-OMeTAD solution at 4000 r.p.m. for 30s followed by evaporation of 100 nm gold electrode on the top of the cell. For the 3D MAPbI₃ film preparation, the precursors (PbI₂:MAI=1:1) solution (DMSO:GBL=3:7, 1.2M) was spin-cast on FTO/TiO₂ substrates and chlorobezene dripping method was used. The MAPbI₃ films were then annealed at 100 °C for 10 minutes.

Characterization

Optical metrology: UV-Visible absorption spectra were acquired on a PerkinElmer UV-Lambda 950 instrument. Steady-state Photoluminescence (PL) (excitation at 532 nm) and time-resolved photoluminescence (TRPL) (excitation at 405 nm and emission at 760 nm) were measured with Edinburgh Instruments Ltd (FLS980).

Atomic force microscopy (AFM): Topography images and Work Function (WF) were acquired on Bruker Dimension ICON instrument. The work function of samples was measured by KPFM. Conducting AFM tips (SCMPIT/PtIr, Bruker, USA) used for this study had a typical spring constant of 2.8 N m⁻¹ and a resonance frequency of 75 kHz. Typical scan line frequency was 0.3 Hz and each image contained 512 × 512 pixels. Fresh Au film was used for work function calculation.

Scanning electron microscopy (SEM) imaging was conducted on a field emission scanning electron microscopy (FE-SEM; SU-8020, Hitachi) at an acceleration voltage of 3 keV.

X-Ray energy dispersive spectroscopy (EDS) analysis was performed at a X-Ray energy dispersive spectrometer (EMAX evolution X-Max 80/EX-270, Horiba) at an acceleration voltage of 20 keV.

X-ray diffraction (XRD) measurements were carried out in a θ - 2θ configuration with a scanning interval of 2θ between 3° and 45° on a Rigaku Smart Lab (X-ray Source: Cu K α ; $\lambda = 1.54 \text{ \AA}$).

Grazing incidence wide angle X-ray scattering (GIWAXS) measurements were performed at D-line at the Cornell High Energy Synchrotron Source (CHESS). The wavelength of the X-rays was 1.166 \AA with a bandwidth $\Delta\lambda/\lambda$ of 1.5%. The scattering signal was collected by Pilatus 200K detector, with a pixel size of $172 \mu\text{m}$ by $172 \mu\text{m}$ placed at 176.76 mm away from the sample position. The incident angle of the X-ray beam was at 0.25 degree and the integration time was 1s . Time resolved GIWAXS was measured during spin coating with the exposure time of 0.2 seconds. This enabled us to capture the phase changes during the coating process accurately as shown previously. Kapton tape was employed to keep the detector safe from the splashing.

X-ray photoelectron spectroscopy (XPS) measurements were acquired on Thermo Fisher Scientific (K-Alpha) (X-ray source: Al K α ; pressure: $1 \times 10^{-8} \text{ Pa}$).

Solar cell characterizations: The J-V performance of the perovskites solar cells were analyzed by Keithley 2400 source under ambient condition at room temperature, and the illumination intensity was 100 mW cm^{-2} (AM 1.5G Oriel solar simulator). The

scan rate was 0.3 V s^{-1} . The delay time was 10 ms; and the scan step was 0.02 V. The power output of lamp was calibrated by a NREL-traceable KG5 filtered silicon reference cell. The device area of 0.09 cm^2 is defined by a metal aperture to avoiding light scattering from the metal electrode into the device during the measurement.

5 The EQE was characterized on the QTest Station 2000ADI system (Crowntech. Inc., USA), and the light source is a 300 W xenon lamp. The monochromatic light intensity for EQE was calibrated with a reference silicon photodiode.

Mobility measurement: Electron-only devices (FTO/TiO₂/Cs_x-2D perovskites/PCBM/Ag) were fabricated to calculate the electron mobility of the
10 samples. The dark *J-V* characteristics of the electron-only devices were measured by a Keithley 2400 source. The mobility is extracted by fitting the *J-V* curves by the Mott-Gurney equation.

Contact angle measurements were conducted on Dataphysics OCA-20 with a drop of ultrapure water (0.05 mL). The photographs were taken 1 second after water
15 dripping.

X-ray photoelectron spectroscopy (XPS) analysis

Since doping ratio doesn't represent the final composition in the crystal for some system, it's therefore important to know the exactly Cs⁺ ratio in the final doped 2D (BA)₂Cs_{3x}(MA)_{3-3x}Pb₄I₁₃ crystal. Herein we performed X-ray photoelectron spectroscopy (XPS) analysis on the Cs₁₅-2D ((BA)₂Cs_{0.45}(MA)_{2.55}Pb₄I₁₃) film to provide correct doping ratio in the crystal. Considering possible desorption of organic molecules from the crystal under the high vacuum environment, we focus on ratio Cs/Pb ratio to determine the Cs concentration in the final film. The calculated Cs/Pb ratio in the solution is 0.1125:1, which is pretty closed the Cs/Pb ratio determined from XPS analysis for the final film (0.1145:1). The result suggests that the Cs⁺ doping concentration in solution was retained after solution-to-solid transformation.

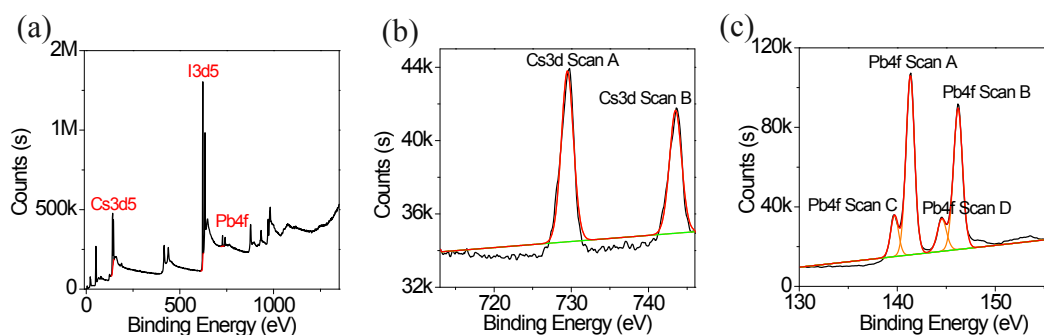


Fig. S1. (a) X-ray photoelectron spectroscopy (XPS) of the Cs₁₅-2D film. (b) and (c) showing Cs and Pb spectrum, respectively.

15

Table S1. The Cs/Pb atomic ratio determined from XPS analysis and calculation.

Atomic ratio	XPS analysis	Calculation
		n

Cs/Pb	0.1144:1	0.1125:1
-------	----------	----------

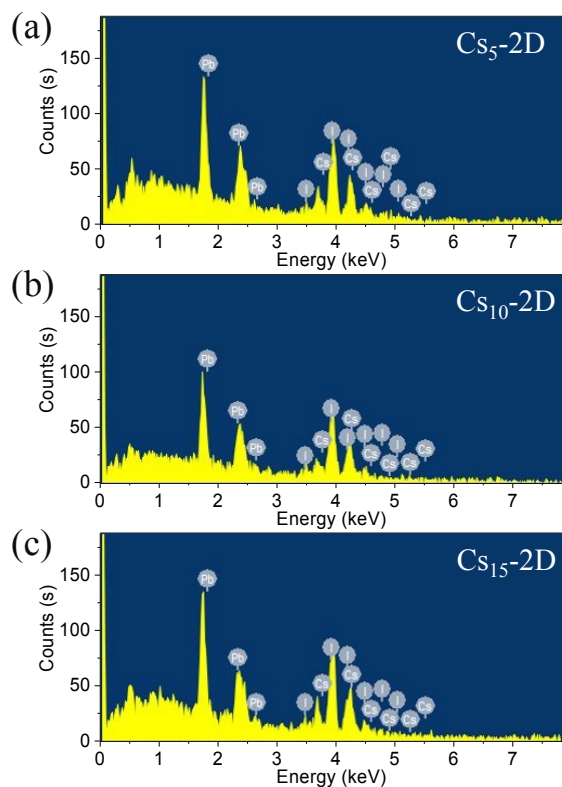


Fig. S2. X-Ray Energy Dispersive Spectroscopy (EDS) of the Cs_x-2D films: (a) Cs₅-2D, (b) Cs₁₀-2D and (c) Cs₁₅-2D.

5 Table S2. The Cs/Pb atomic ratio determined from EDS analysis and calculation. Note that the obtained quantity is more accurate for films with higher Cs⁺ doping concentration due to enough signals required.

Atomic ratio (Cs/Pb)	Cs ₅ -2D	Cs ₁₀ -2D	Cs ₁₅ -2D
EDS analysis	0.0589:1	0.0836:1	0.1182:1
Calculation	0.0375:1	0.0750:1	0.1125:1

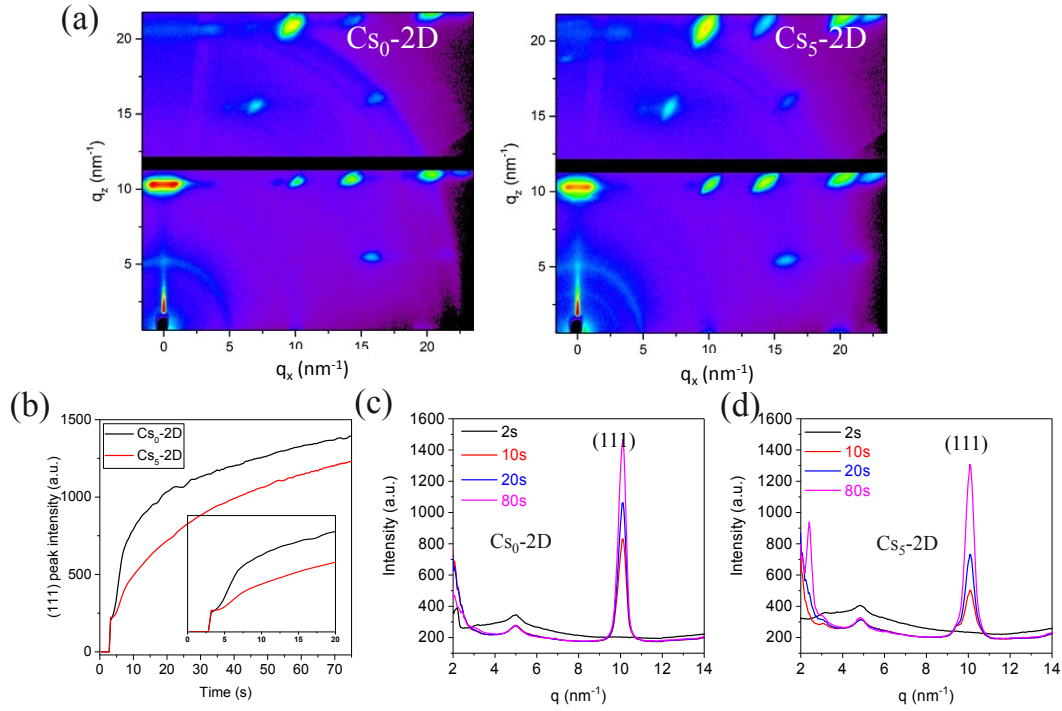


Fig. S3. (a) 2D GIWAXS snapshots taken at the end of spin-coating (20 sec) for the Cs₀-2D and Cs₅-2D samples. (b) The integrated intensity traces associated to the (111) reflection of the perovskite phase during long-term solution-solid transformation (80 s). Inset showing the evolution during spin-coating (20 sec). (c) Out-of-plane profiles of GIWAXS patterns for Cs_x-2D films at different times during long-term solution-solid transformation: (c) Cs₀-2D, (d) Cs₅-2D.

Table S3. FWHM of the (111) peak for Cs_x-2D films at different time during solution-solid transformation.

FWHM (nm ⁻¹)	10 s	20 s	80 s
Cs ₀ -2D	0.46	0.45	0.43
Cs ₅ -2D	0.68	0.55	0.5

2D crystalline structure analysis

Based on theoretical calculation^[1] and XRD analysis of the $(\text{BA})_2(\text{MA})_{n-1}\text{Pb}_n\text{I}_{3n+1}$ ($n=1-4$) (shown in Fig. S4 below), we found that the diffraction pattern of perovskite varies with n . For example, crystals exhibit characteristic diffraction peaks at 14.23° ((111) plane) for the $n=4$, 14.07° ((111) plane) for the $n=3$, 4.44° ((020) plane) for the $n=2$, and 6.42° ((002) plane) for the $n=1$. Our XRD and GIWAXS results confirm phase-pure crystal, without any signals from $n=1, 2, 3$ phases. Meanwhile, phase pure 2D crystals can also be distinguished from optical analysis. For example, crystals with a mixture of n present a mixture of peaks in PL and absorption spectra.^[2] While our optical results clearly indicate a single-peak in PL. It thus implies that the 2D crystal fabricated in our work is phase-pure ($n=4$).

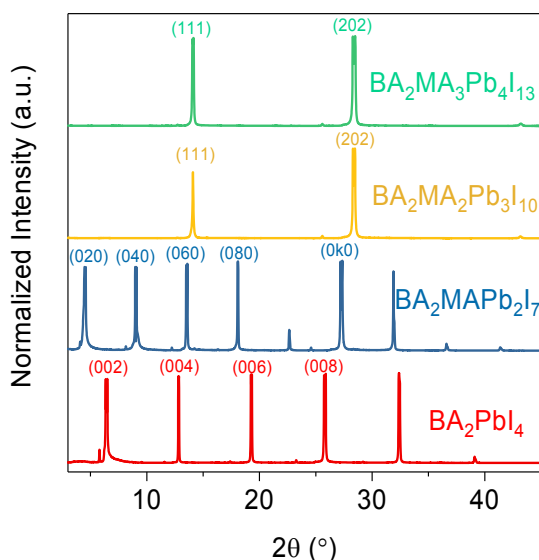


Fig. S4. XRD patterns of crystals $(\text{BA})_2(\text{MA})_{n-1}\text{Pb}_n\text{I}_{3n+1}$ ($n=1-4$).

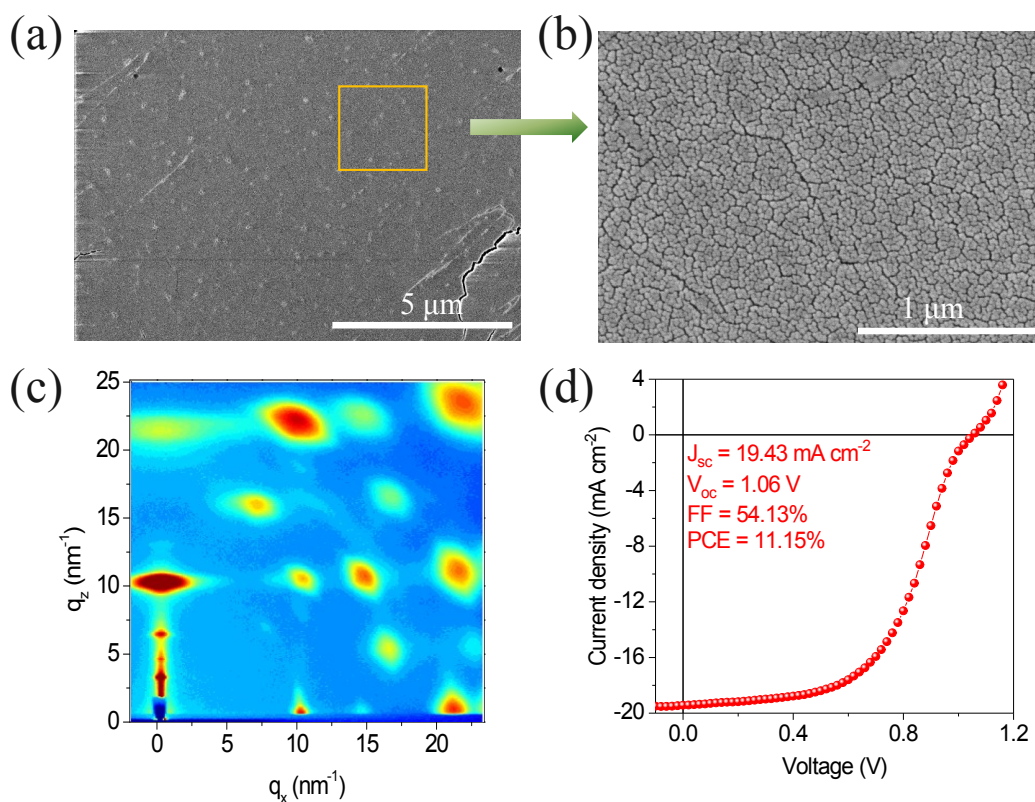


Fig. S5. (a) Low magnification and (b) high magnification SEM images showing granular grains and plenty of gaps on the 2D $(\text{BA})_2(\text{MA})_3\text{Pb}_4\text{I}_{13}$ film when cast from neat DMF solvent. (c) GIWAXS pattern of the 2D $(\text{BA})_2(\text{MA})_3\text{Pb}_4\text{I}_{13}$ film cast from neat DMF solvent. (d) J - V curve for the peak efficiency of 11.15% for the $(\text{BA})_2(\text{MA})_3\text{Pb}_4\text{I}_{13}$ film cast from neat DMF solvent.

Apparently, the $(\text{BA})_2(\text{MA})_3\text{Pb}_4\text{I}_{13}$ film cast from neat DMF solvent exhibits worse film quality and crystalline behavior than that cast from solvents mixture. The observations of granular grains and plenty of gaps of the film cast from neat DMF solvent are similar with what have been reported by Mohite et al.^[3] Furthermore,

both elongated crystalline peaks and phase-impurity were observed for the film cast from neat DMF solvent, i.e., an appearance of peak at $q=6.9 \text{ nm}^{-1}$. The worse film quality and crystalline behavior therefore lead to lower FF and overall PCE of the device in contrast to the sample cast from solvents mixture.

5

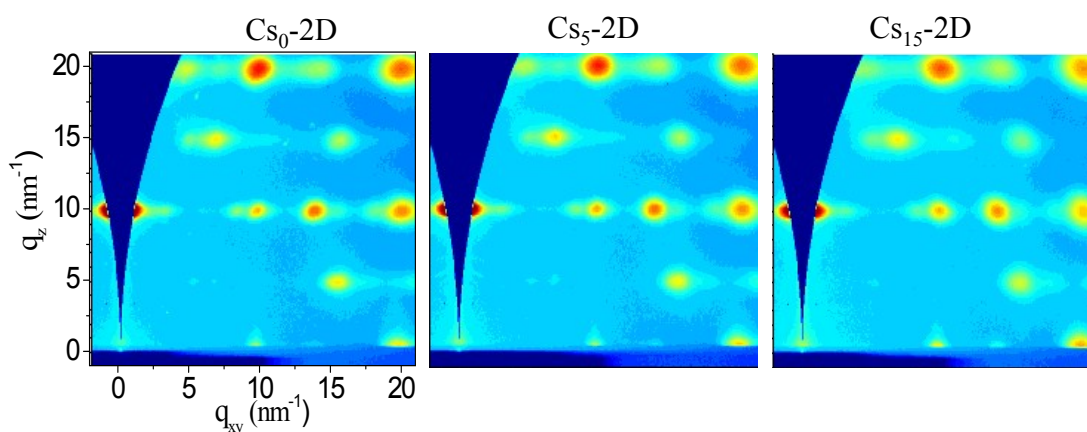
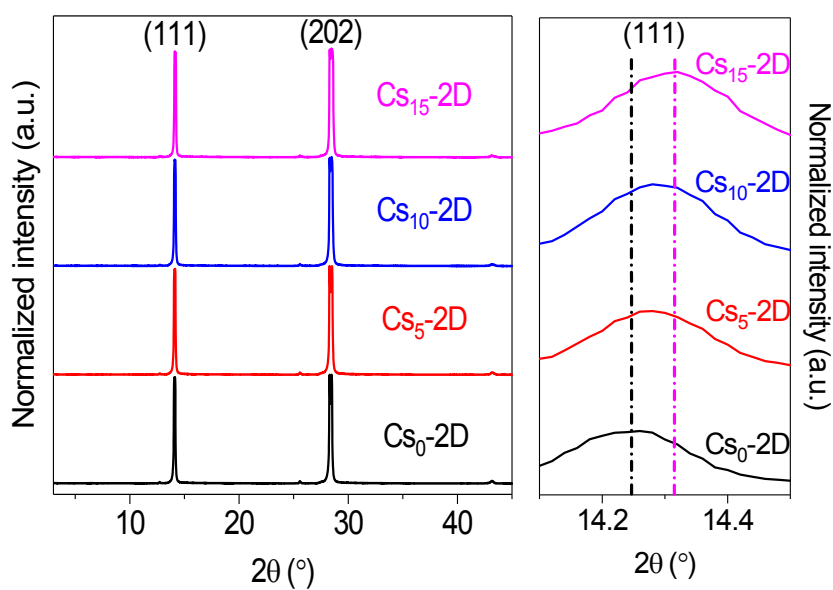


Fig. S6. Grazing incidence wide-angle X-ray scattering (GIWAXS) showing films retain perfect crystal orientation and 2D crystalline nature after Cs^+ doping.



10

12

Fig. S7. Comparison of X-ray diffraction (XRD) of the $\text{Cs}_x\text{-2D}$ perovskite films. The right section shows shift of the (111) peak with increased Cs^+ doping content.

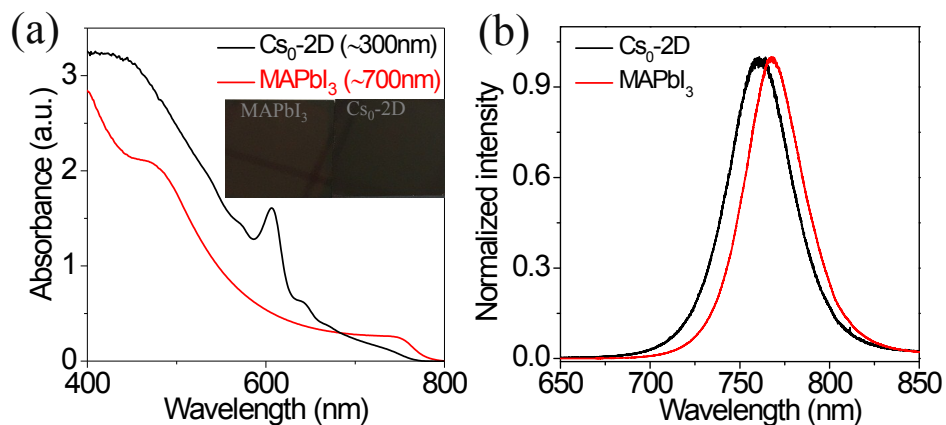
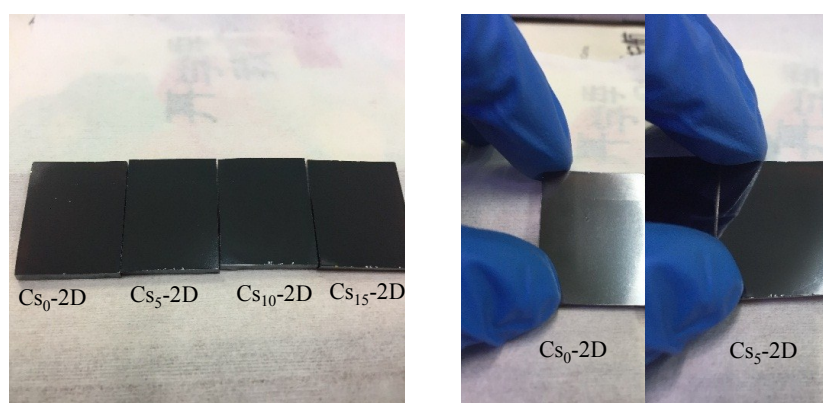


Fig. S8. (a) UV-Vis absorption of Cs_0 -2D film (ca. 700 nm) and 3D MAPbI_3 film (ca. 300 nm). Inset showing the photos of Cs_0 -2D film (ca. 700 nm) and 3D MAPbI_3 film (ca. 300 nm). Compared to the 3D MAPbI_3 film, the 2D films looks darker due to higher
 5 absorption intensity. The absorption of 2D film shows a cutoff at ca. 770 nm which is ca. 16 nm lower in contrast to that of the 3D film. (b) Normalized PL spectra showing peaks of ca. 760 nm for the Cs_0 -2D film and ca. 768 nm for the 3D MAPbI_3 film, respectively.



10

Fig. S9. Photos of Cs_x -2D perovskite films. All films look dark; while the Cs_5 -2D film looks more shining in contrast to the Cs_0 -2D film.

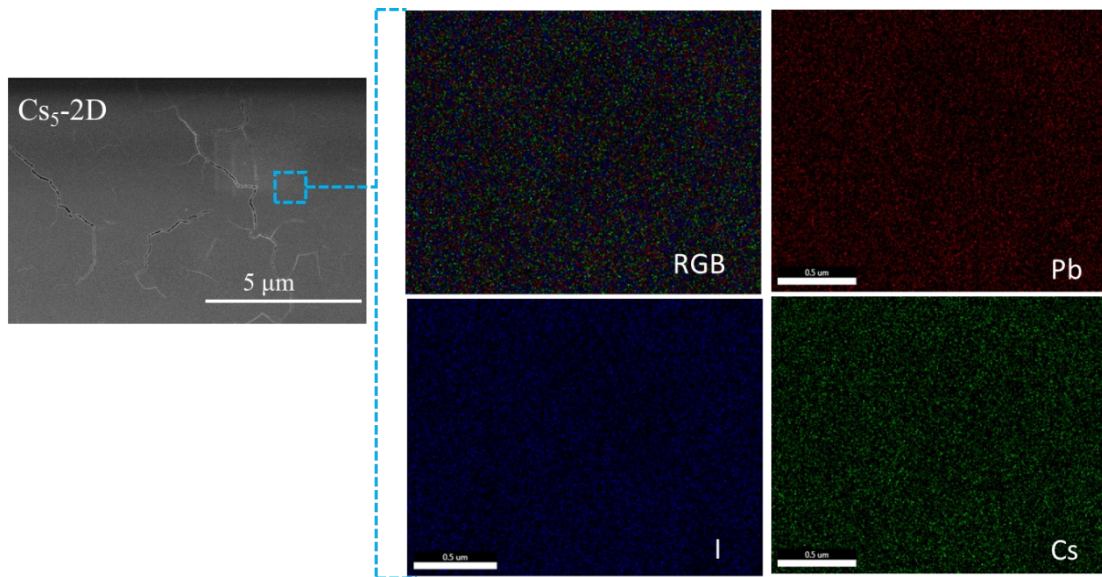


Fig. S10. Elemental analysis by scanning electron microscopy (SEM) with X-Ray Energy Disperse Spectrometer (EDS) mapping on the Cs₅-2D film showing uniform Cs⁺ doping.

5

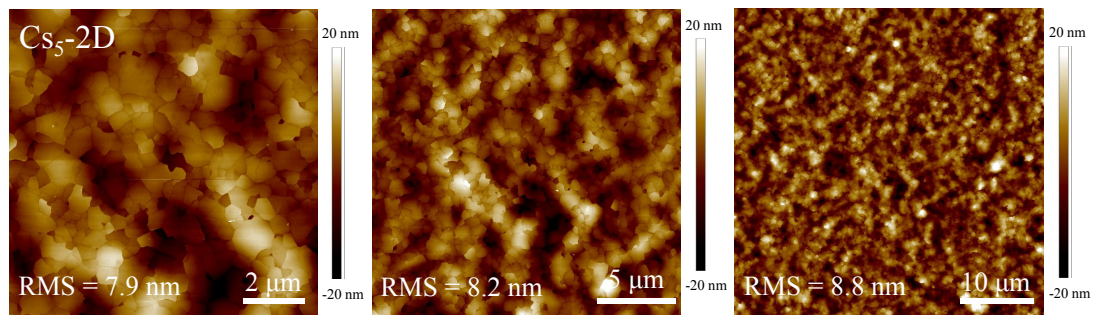


Fig. S11. Different magnification AFM images of the Cs₅-2D perovskite films showing quite closed root-mean-square roughness (RMS).

10

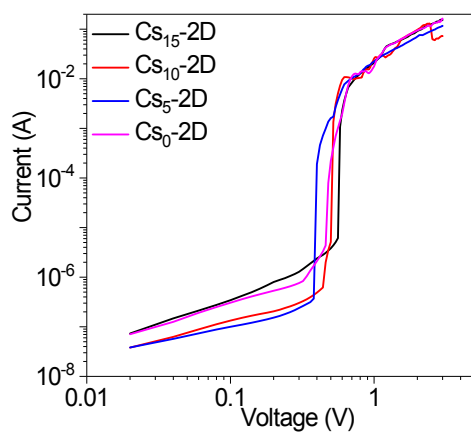


Fig. S42. Dark current-voltage measurement of the electron-only devices for all Cs_x -2D perovskites displaying V_{TFL} kink point behavior.

5

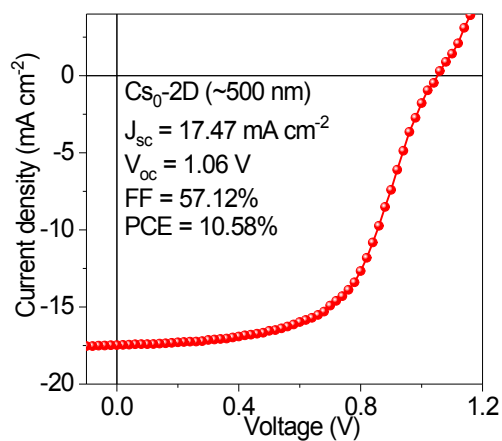


Fig. S5. J - V curve of the Cs_0 -2D perovskite solar cell based on thinner film (ca. 500 nm). Thinner film yields decreased J_{sc} and overall PCE when compared to the device of ca. 700 nm film.

10

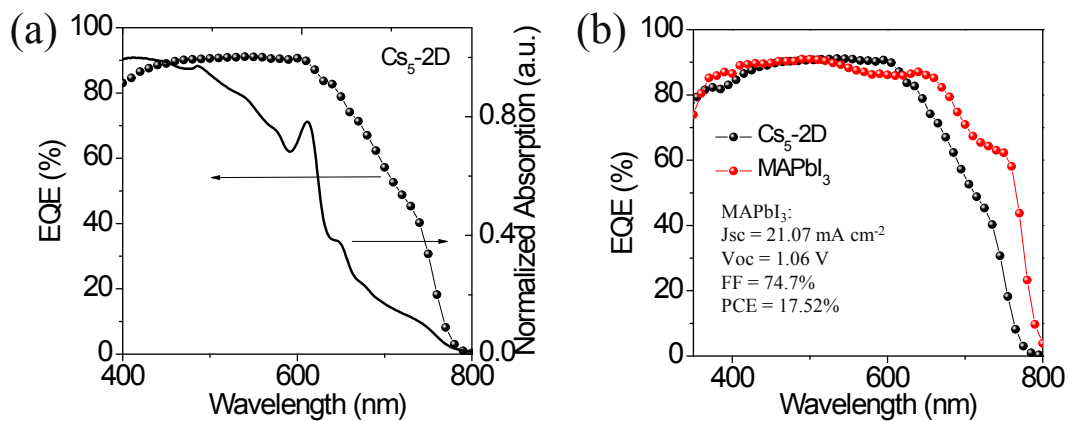
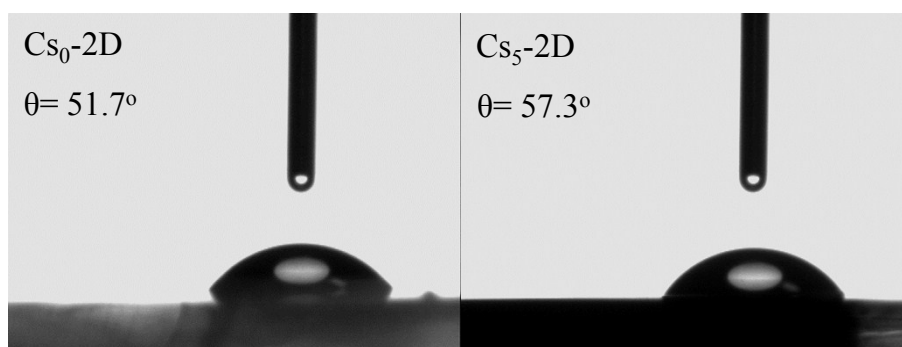


Fig. S64. (a) EQE and absorption spectra showing the same cutoff at ca. 768 nm. (b) EQE for both $\text{Cs}_5\text{-2D}$ and 3D MAPbI_3 with PCE of 17.52% fabricated with same device architecture illustrating difference. A faster decline in EQE intensity above ca. 630 nm was observed for the $\text{Cs}_5\text{-2D}$ device, which could be attributed to faster decrease in the absorption intensity.



10 Fig. S15. Contact angle of water showing more hydrophobic surface of the $\text{Cs}_5\text{-2D}$ films in contrast to the $\text{Cs}_0\text{-2D}$ films. The average contact angle is $51.0 \pm 1.2^\circ$ for the $\text{Cs}_0\text{-2D}$ film while $56.8 \pm 0.9^\circ$ for the $\text{Cs}_5\text{-2D}$ film.

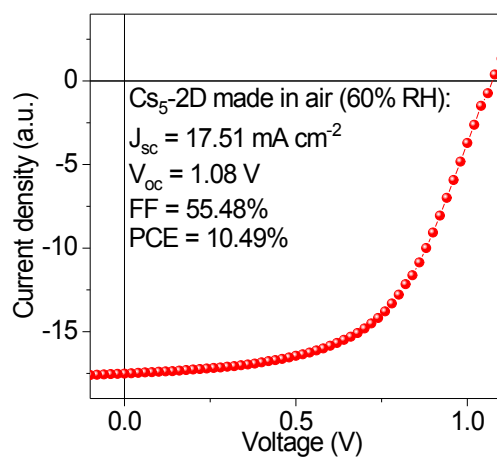


Fig. S16. *J-V* curve of the Cs₅-2D perovskite solar cell fabricated in air with 60% RH. Compared to the peak efficiency obtained in N₂-glove box, worse performance of the device fabricated in air is attributed to slight decreases in *J_{sc}* and *FF*.

5

Reference

- 1 D. H. Cao, C. C. Stoumpos, O. K. Farha, J. T. Hupp and M. G. Kanatzidis, *J. Am. Chem. Soc.*, 2015, **137**, 7843-7850.
- 2 J. Liu, J. Leng, K. Wu, J Zhang and S. Jin, *J. Am. Chem. Soc.*, 2017, **139**, 1432-1435.
- 10 3 H. Tsai, W. Nie, J.-C. Blancon, C. C. Stoumpos, R. Asadpour, B. Harutyunyan, A. J. Neukirch, R. Verduzco, J. J. Crochet, S. Tretiak, L. Pedesseau, J. Even, M. A. Alam, G. Gupta, J. Lou, P. M. Ajayan, M. J. Bedzyk, M. G. Kanatzidis and A. D. Mohite, *Nature*, 2016, **536**, 312-316.